frontiers in Materials

ORIGINAL RESEARCH
published: 28 January 2022
doi: 10.3389/fmats.2022.838648

The Thermal and Electronic Properties of the Lateral Janus MoSSe/WSSe Heterostructure

Zhongliang Shen[1], Kai Ren[2], Ruxing Zheng[2], Zhaoming Huang[3], Zhen Cui[4], Zijun Zheng[1] and Li Wang[5]*

[1]School of Mechatronic Engineering, Zhejiang Business Technology Institute, Ningbo, China, [2]School of Mechanical and Electronic Engineering, Nanjing Forestry University, Nanjing, China, [3]School of Mechanical Engineering, Wanjiang University of Technology, Maanshan, China, [4]School of Automation and Information Engineering, Xi'an University of Technology, Xi'an, China, [5]School of Electromechanical and Automotive Engineering, Xuancheng Vocational and Technical College, Xuancheng, China

Two-dimensional materials have opened up extensive applications for traditional materials. In particular, heterostructures can further create fantastic performances. In this investigation, the lateral heterostructure was constructed using Janus MoSSe and WSSe monolayers with armchair and zigzag interfaces. Performing first-principles calculations and molecular dynamics simulation method, the thermal stability and the semiconductor characteristics with the type-II band structure to separate the photogenerated charges of such Janus MoSSe/WSSe heterostructure are presented, which suggests the potential application of acting as a photocatalyst for water splitting. Importantly, the asymmetric interface of the Janus MoSSe/WSSe heterostructure can result in natural bending, which limits the heat flow transport. Smaller heat flow and the interfacial thermal resistance of the lateral MoSSe/WSSe heterostructure with a zigzag edge interface are mainly due to suppressed acoustic branches. These structural symmetry and interface-dependent properties show the future applications in photovoltaic and thermoelectric devices.

Keywords: two-dimensional material, type-II band structure, interfacial thermal resistance, lateral MoSSe/WSSe heterostructure, applications

OPEN ACCESS

Edited by:
Guangzhao Wang,
Yangtze Normal University, China

Reviewed by:
Hao Guo,
Hebei Normal University of Science and Technology, China
Kezhen Qi,
Shenyang Normal University, China

****Correspondence:***
Zhaoming Huang
jimmymacy@163.com

Specialty section:
This article was submitted to Computational Materials Science, a section of the journal Frontiers in Materials

Received: *18 December 2021*
Accepted: *07 January 2022*
Published: *28 January 2022*

Citation:
Shen Z, Ren K, Zheng R, Huang Z, Cui Z, Zheng Z and Wang L (2022) The Thermal and Electronic Properties of the Lateral Janus MoSSe/WSSe Heterostructure. Front. Mater. 9:838648. doi: 10.3389/fmats.2022.838648

INTRODUCTION

After graphene was discovered (Geim and Novoselov, 2010), it has frequently demonstrated some novel properties due to its very special monolayer structure (Butler et al., 2013; Kim et al., 2015; Xu et al., 2015; Wei et al., 2016; Gao et al., 2017; Zaminpayma et al., 2017; Zhang et al., 2018; Zhou et al., 2018; Sun and Schwingenschlögl, 2021a), which has attracted tremendous investigations to explore the other excellent characteristics and applications of two-dimensional (2D) materials (Li et al., 2014; Li et al., 2019; Li et al., 2021; Vahedi Fakhrabad et al., 2015; Keyte et al., 2019; Xu et al., 2020; Ren et al., 2021a; Ren et al., 2021b; Sun et al., 2021). For instance, biphenylene, a graphene-like material, was prepared, which is metallic, instead of dielectric (Fan et al., 2021). Biphenylene also possesses excellent electronic, mechanical, and catalytic properties (Luo et al., 2021). Two-dimensional $MoSi_2N_4$ was synthesized by chemical vapor deposition, suggesting a sandwiched structure; the exhibited semiconducting nature was also investigated, with a bandgap of about 1.94 eV (Hong et al., 2020). A novel 2D material of transition metal dichalcogenides (TMDs) has attracted considerable focus (Luo et al., 2019a; Luo et al., 2019b; Dongqi et al., 2021). For example, WSe_2 has been proved to

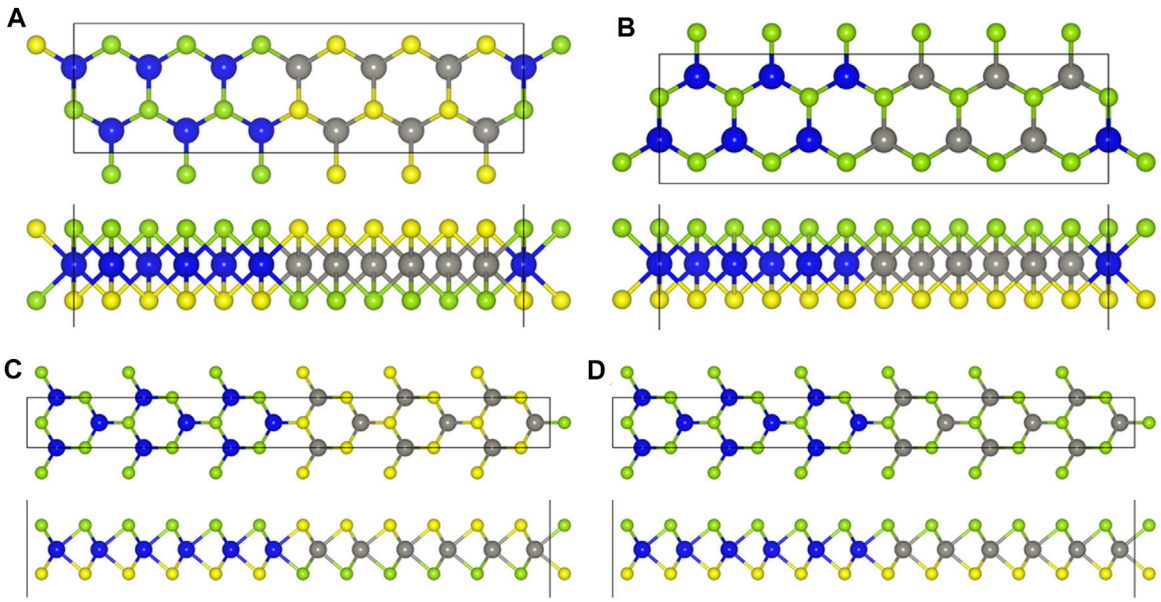

FIGURE 1 | Crystal structure of the **(A)** arm-1, **(B)** arm-2, **(C)** zig-1, and **(D)** zig-2 MoSSe/WSSe heterostructures; the blue, gray, cyan, and yellow are Mo, W, Se, and S atoms, respectively.

be a semiconductor material with indirect bandgap, high carrier mobility, remarkable optical properties, and the responsivity of the field effect transistor of this material in the visible wavelength range is of 10^{-1}–10^{5}A/W (Zhao et al., 2013; Allain and Kis, 2014; Jo et al., 2018). $MoSe_2$ is a layered material possessing a bandgap of 1.55 eV. It is found that $MoSe_2$ has strong light absorption capacity and photoelectric conversion efficiency (close to 10%) in the range of visible light and has a great application prospect in photovoltaic devices (Ma et al., 2011; Shi et al., 2013; Liu et al., 2016a). All these remarkable performances of the 2D materials present advanced applications in metal-ion batteries (Sun and Schwingenschlögl, 2020; Sun and Schwingenschlögl, 2021b), photocatalyst (Ong, 2017; Ren et al., 2019; Ren et al., 2021c; Sun et al., 2020; Agarwal et al., 2021), photodiode (Ouyang et al., 2021), light emitting devices (Ren et al., 2021d), etc.

Interestingly, these novel performances of the 2D materials can also be adjusted by suitable methods, such as external strain (Wang et al., 2019a; Shu, 2021; Zhao et al., 2021), electric field (Sun et al., 2017; Cui et al., 2021a), adsorption (Cui et al., 2021b), doping (Cui et al., 2021a), and defect (Sun et al., 2019). Recently, the synthesis of heterostructures demonstrates further properties and applications (Novoselov et al., 2016; Ang and Ang, 2019; Chen et al., 2020; Hidding and Guimarães, 2020). It is worth noting that a 2D heterostructure can be divided into a vertical heterostructure and a lateral heterostructure. The former can be obtained by artificial fixed-point transfer and chemical vapor deposition (CVD), and the latter is obtained by CVD epitaxial growth (Ding et al., 2018; Jiang, 2018). A vertical heterostructure is a structure that connects two or more layered materials through van der Waals (vdW) force, which can induce astonishing performances across the interface. For instance, the carrier mobility of a ZnO/BSe vertical heterostructure is as high as 2538.16 $cm^2 \cdot v^{-1} \cdot s^{-1}$, which is higher than that of original ZnO (360.88 $cm^2 \cdot v^{-1} \cdot s^{-1}$) and BSe (419.01 $cm^2 \cdot v^{-1} \cdot s^{-1}$) (Ren et al., 2020a). The Z-Scheme photocatalytic mechanism was discovered in the $MoSe_2/HfS_2$ heterostructure and is used as an efficient photocatalyst for water splitting (Wang et al., 2019b). Nevertheless, due to the weak vdW force between layers, the vertical heterostructure will be unstable at high temperature and other extreme conductance; thus, Duan et al. synthesized MoS_2/$MoSe_2$ and WS_2/WSe_2 lateral heterostructures by using the CVD epitaxial growth method and proved that the lateral heterostructure can be formed with remarkable current rectification behavior (Duan et al., 2014). The MoS_2/WSe_2 lateral heterostructure was studied that the fracture strength was determined by the mechanical properties of MoS_2. When the temperature increases from 50 to 500 K, the fracture strength and strain of MoS_2/WSe_2 vdW heterostructure are reduced by about 35 and 36%, respectively (Qin et al., 2019). More recently, the TMD material with a Janus structure, MoSSe, was successfully prepared (Lu et al., 2017), which exhibits novel electronic and optical properties (Ren et al., 2020b). WSSe with a Janus structure also have unexpected properties (Lou et al., 2021). WSSe with an armchair edge nanotube has strong oxidation ability, resulting in high conversion efficiency of solar hydrogen production (Guo et al., 2020). Considering that both monolayers MoSSe and WSSe have outstanding properties, and the MoSSe/WSSe heterostructure was also recently prepared (Trivedi et al., 2020), the lateral MoSSe/WSSe heterostructure was selected to explore the interesting performances and potential applications.

In this investigation, the Janus MoSSe and WSSe monolayers are selected to construct lateral heterostructures by armchair and zigzag edges as interfaces. The stability of the Janus MoSSe/WSSe heterostructure is addressed by using the molecular dynamics

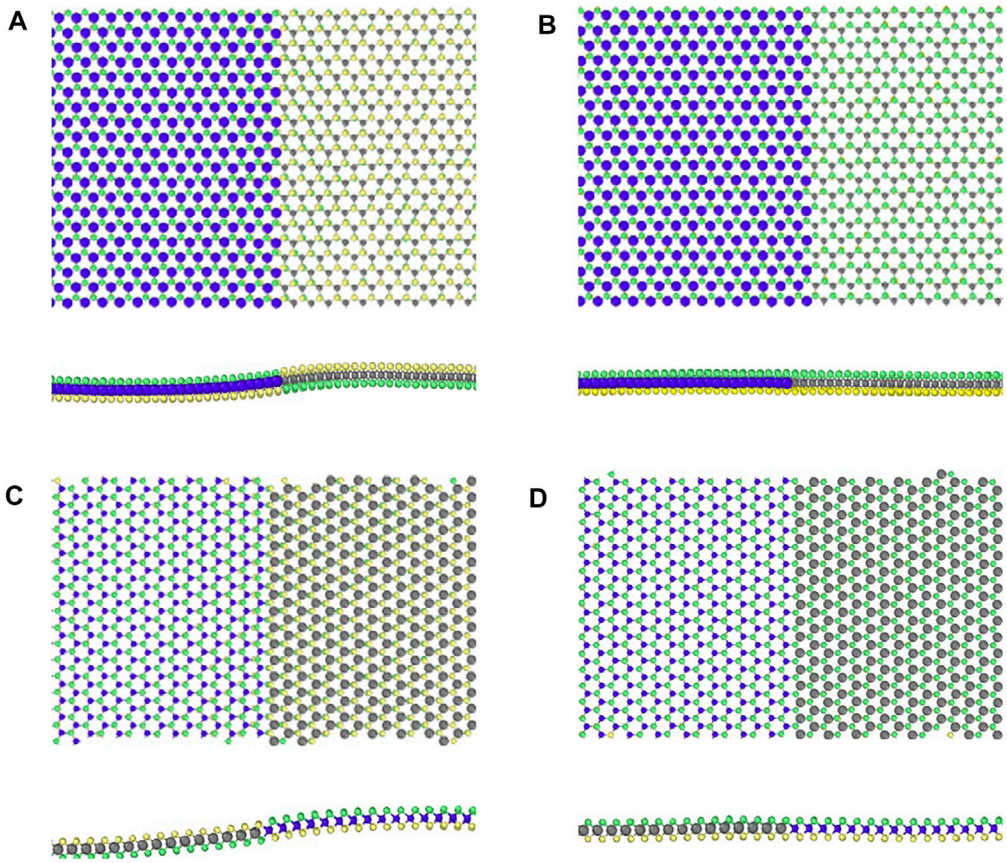

FIGURE 2 | MD snapshot for the structures of the **(A)** arm-1, **(B)** arm-2, **(C)** zig-1, and **(D)** zig-2 MoSSe/WSSe heterostructures at 300 K.

(MD) method. Then, electronic properties of the type-II band alignment of the MoSSe/WSSe heterostructure are obtained using first-principles calculations. Importantly, the structural symmetry and interface edge dependence for the thermal performance are further investigated.

COMPUTATIONAL METHODS

For the first-principles calculations, the simulations were conducted by the Vienna *ab initio* simulation package (VASP) based on density functional theory (DFT) (Capelle, 2006). The generalized gradient approximation (GGA) and the projector augmented wave potentials (PAW) were used by the Perdew–Burke–Ernzerhof (PBE) functional for the exchange correlation functional (Kresse and Furthmüller, 1996; Perdew et al., 1996; Kresse and Joubert, 1999). The energy cutoff and the Monkhorst–Pack *k*-point grids were considered to be 550 eV and $17 \times 17 \times 1$, respectively. The thickness of the vacuum energy level was employed by the 25 Å to prevent the interaction of the nearby layers. The studied heterostructures were fully relaxed by the Hellmann–Feynman force smaller than 0.01 eV $Å^{-1}$ for each atom. Furthermore, the convergence of the energy for the systems was controlled within 1×10^{-5} eV. The density functional perturbation theory (DFPT) was used to obtain the phonon spectra of the investigated heterostructure by the PHONOPY code (Togo et al., 2008; Togo and Tanaka, 2015).

The MD calculations were performed by the LAMMPS package (Plimpton, 1995) in this work using parameterized Stillinger–Weber potential to demonstrate the covalent interaction between S, Se, Mo, and W atoms (Jiang, 2018). The time step of our MD simulation was set as 1 fs, and Newton's equations of atomic motion were considered in the velocity Verlet algorithm. First, the studied heterostructure was relaxed for 10 ps under 300 K by the NPT (isothermal and isobaric) ensemble, and then, NVT ensemble was used to further optimize the structure of the system by Nosé–Hoover temperature sustaining 2000 ps. Next, the Janus heterostructure was equilibrated by the NVE (isovolumetric and isoenergetic) (Ren et al., 2020c).

RESULTS AND DISCUSSION

The structure of the lateral MoSSe/WSSe heterostructure is constructed along two interfaces: armchair and zigzag edge. For the MoSSe/WSSe heterostructure with an armchair interface, asymmetric with a Janus structure, S and Se can be

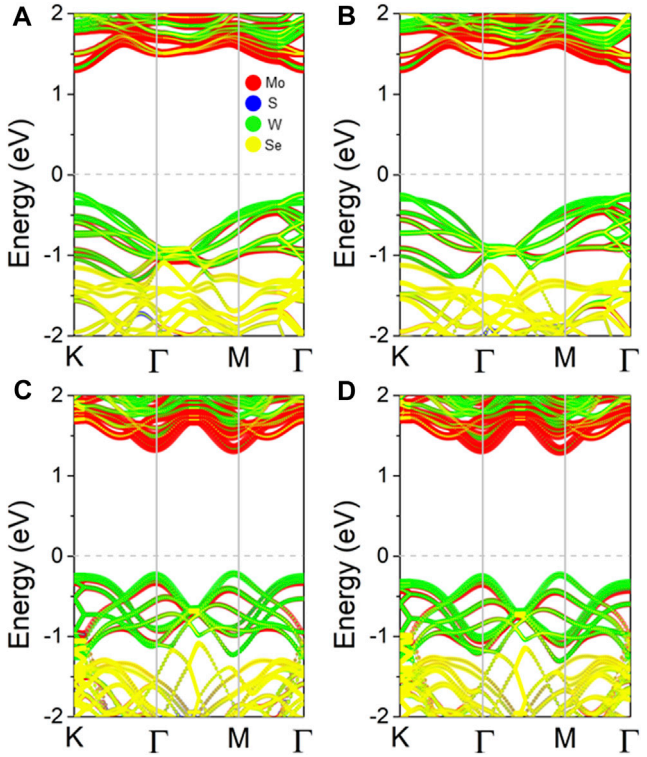

FIGURE 3 | Projected band structures of the **(A)** arm-1, **(B)** arm-2, **(C)** zig-1, and **(D)** zig-2 MoSSe/WSSe heterostructures.

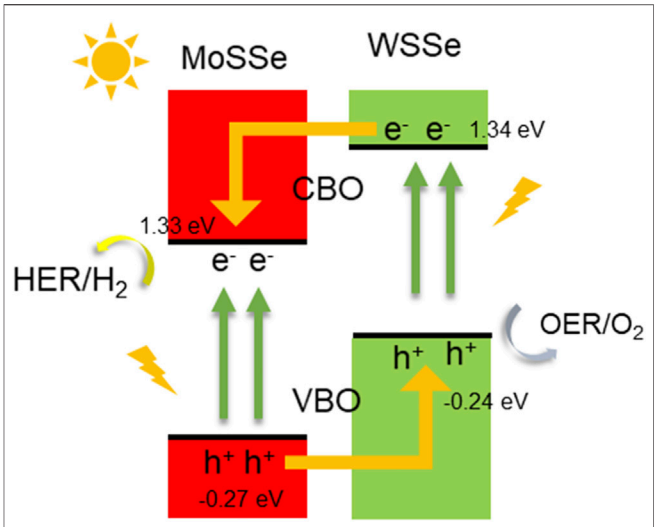

FIGURE 4 | Schematic of the exciton migration mode of the lateral MoSSe/WSSe heterostructure.

arranged on both sides of Mo (or W) atoms and the same layer, namely, arm-1 and arm-2, as shown in **Figures 1A,B**, respectively. Similarly, the zig-1 and zig-2 are shown in **Figures 1C,D**, respectively. Besides, the MoSSe and WSSe monolayers are also optimized by the lattice constants of 3.23 and 3.27 Å, respectively. The obtained bond lengths of the Mo–S, Mo–Se, W–S, and W–Se in the optimized monolayered MoSSe and WSSe are 2.41, 2.53, 2.43 and 2.54 Å, respectively, which are agreement with the experimental work, 2.58 and 2.41 Å for Mo–Se and Mo–S, respectively (Lu et al., 2017). Thus, the lattice mismatch of the MoSSe/WSSe heterostructure with armchair and zigzag edges is 3.7 and 2.8%, respectively. Furthermore, the calculated formation energies of arm-1, arm-2, zig-1, and zig-2 MoSSe/WSSe heterostructures are 0.136, 0.095, 0.364, and 0.050 eV, respectively.

To assess the thermal stability of such a lateral MoSSe/WSSe heterostructure, molecular dynamics simulations were employed. After complete relaxation of the lateral MoSSe/WSSe heterostructure at a Nosé–Hoover temperature of 300 K, the structures of arm-1, arm-2, zig-1, and zig-2 lateral MoSSe/WSSe heterostructures are demonstrated in **Figures 2A–D**, respectively. The whole optimization process took about 4000 ps for the lateral MoSSe/WSSe heterostructure, and one can find that the structures of these heterostructures are still intact. Interestingly, at the interface of the arm-1 and zig-1 of the lateral MoSSe/WSSe heterostructure, a bending phenomenon occurred because of the asymmetric atomic arrangement pattern of the S and Se atoms. In detail, this natural folding phenomenon is also caused by the uneven stress of bonds at the interface.

The projected band structure of arm-1, arm-2, zig-1, and zig-2 lateral MoSSe/WSSe heterostructures is shown in as **Figures 3A–D**, respectively. It can be seen that arm-1 and arm-2 lateral MoSSe/WSSe heterostructures possess similar band structures with the semiconductor characteristic with a direct bandgap of 1.57 and 1.58 eV, respectively, suggesting the conduction band minimum (CBM) and valence band maximum (VBM) located at K point. The zig-1 and zig-2 lateral MoSSe/WSSe heterostructures also have a direct bandgap of 1.56 and 1.56 eV, respectively, with the CBM and VBM at Γ point. Importantly, the red, blue, cyan, and yellow marks represent the band contributions of the Mo, S, W, and Se atoms, respectively, which show that these four Janus lateral heterostructures possess type-II band alignment and that the CBM and VBM resulted from MoSSe and WSSe layers, respectively. Besides, the obtained bandgaps are comparable with those of the reported MoSSe/WSSe heterostructure (about 1.53 eV) (Li et al., 2017).

The obtained type-II band structure of the lateral MoSSe/WSSe heterostructure provides the ability to separate the photogenerated electrons and holes continuously. As **Figure 4** shows, taking the arm-1 MoSSe/WSSe heterostructure as an example, the energy positions are also demonstrated. When the MoSSe/WSSe heterostructure is inspired by light, the photogenerated electrons of the MoSSe and WSSe layers can be stimulated to the conduction band (CB), and the photogenerated holes will result in the valence band (VB). Then, the photogenerated electrons at the CB of the WSSe layer and the photogenerated holes at the VB of the MoSSe layer transfer to the CB of the MoSSe layer and the VB of the WSSe layer by the power of the conduction band offset and valence band offset, named conduction band offset (CBO) and

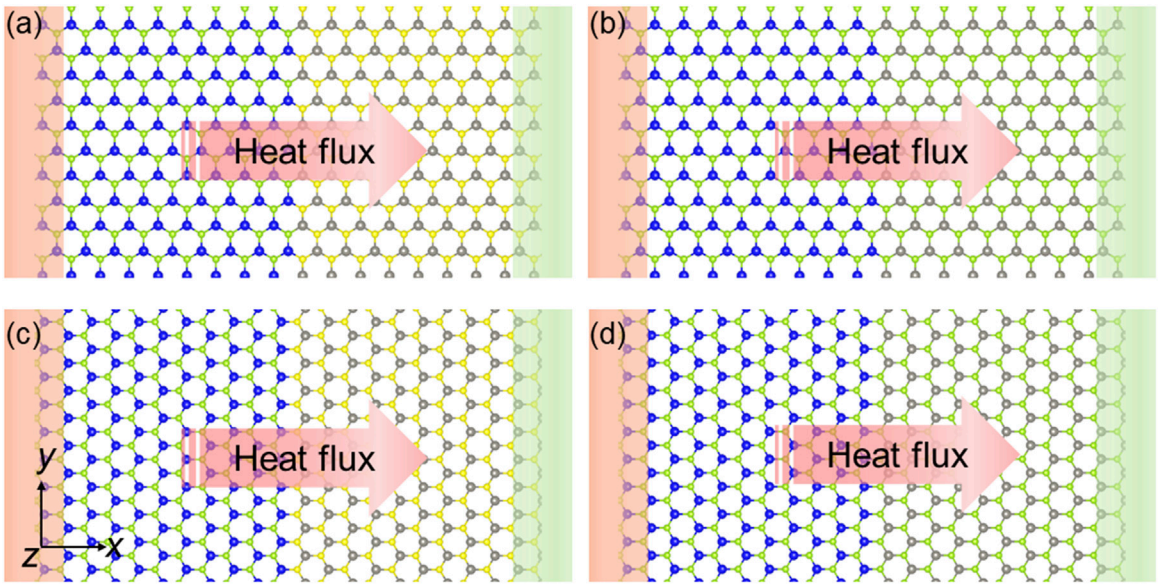

FIGURE 5 | Schematic of the heat transfer style of the **(A)** arm-1, **(B)** arm-2, **(C)** zig-1, and **(D)** zig-2 MoSSe/WSSe heterostructures for the NEMD simulations.

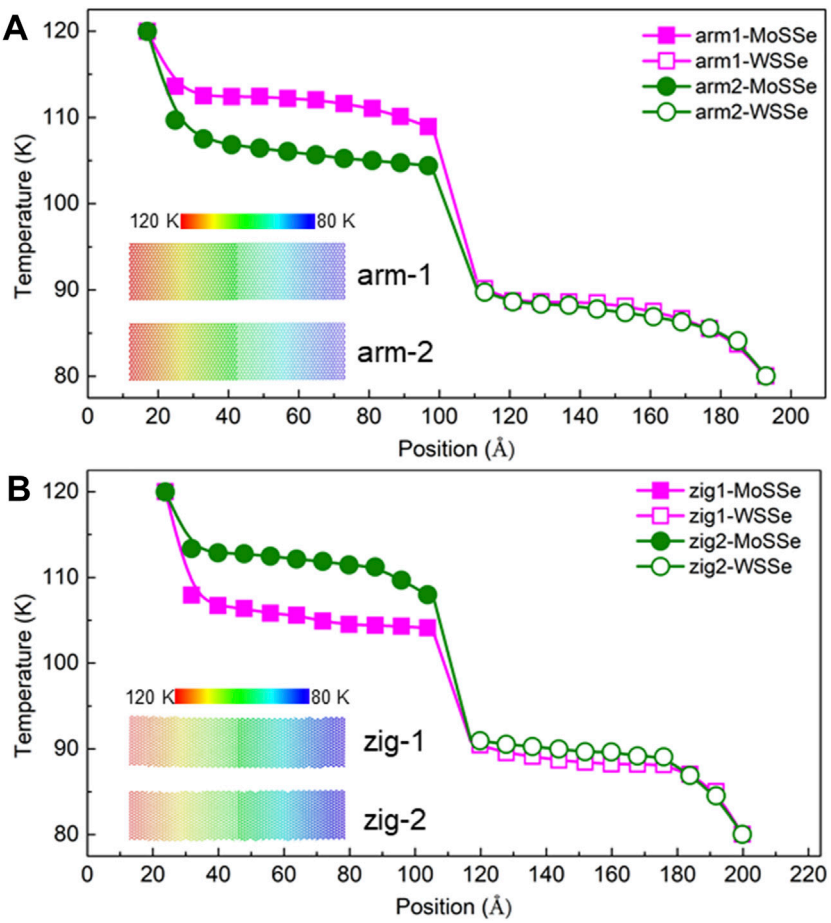

FIGURE 6 | Temperature profiles the **(A)** arm-1, **(B)** arm-2, **(C)** zig-1, and **(D)** zig-2 MoSSe/WSSe heterostructures.

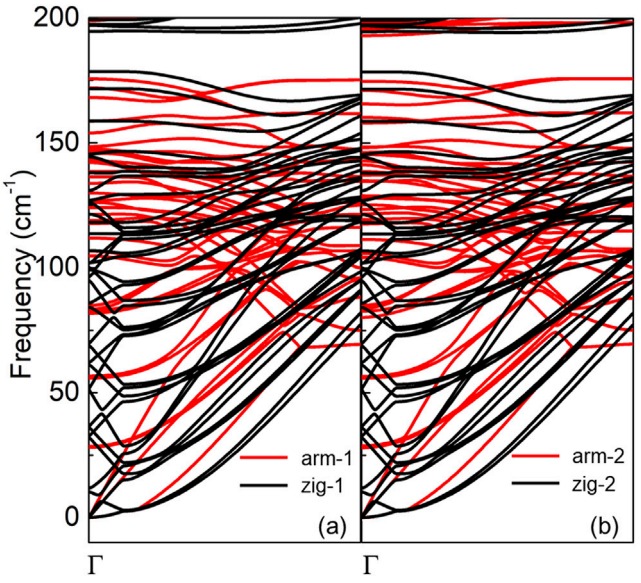

FIGURE 7 | Calculated phonon dispersion for MoSSe/WSSe heterostructure with **(A)** armchair and **(B)** zigzag interface.

valence band offset (VBO) in **Figure 4**, respectively. Thus, the separated photogenerated electrons at the CB of the MoSSe layer and holes at the VB of the WSSe layer can induce the hydrogen evolution reaction (HER) and oxygen evolution reaction (OER), respectively, suggesting these four lateral MoSSe/WSSe heterostructures can act as a potential photocatalyst for water splitting. In particular, if the photogenerated electrons at the CB of the MoSSe layer and the photogenerated holes at the VB of the WSSe layer develop recombination, the HER and the OER are induced at the CB of the WSSe layer and the VB of the MoSSe layer, respectively, and the Z-scheme photocatalytic mechanism is promoted (Xu et al., 2018; Ren et al., 2020d).

To investigate the heat conduction properties of the lateral MoSSe/WSSe heterostructure with different symmetries and interface edges, the non-equilibrium molecular dynamics (NEMD) method was adopted. A temperature gradient is constructed with MoSSe and WSSe acting as cold and hot baths, respectively. The schematic diagram of the temperature gradient of these four heterostructures arm-1, arm-2, zig-1, and zig-2 MoSSe/WSSe is shown in **Figures 5A–D**, respectively, suggesting heat flux flow from the MoSSe layer to the WSSe layer. Besides, NEMD simulations can explain the temperature interaction between atoms. The temperature distribution can also be demonstrated by NEMD calculations across the interface. In MD simulation work Nose–Hoover and Langevin are popular heat baths that can account for different experimental factors (Hu et al., 2020). The Nose–Hoover and Langevin can induce different temperature profiles, and in this NEMD investigation, the temperature jump across the interface of the MoSSe/WSSe heterostructure is critical. Therefore, the Nose–Hoover heat bath was selected. We fixed the ends of the MoSSe and WSSe and set the temperature at 80 and 100 K, respectively. We obtained the time-independent heat flux with enough relaxation time to build a non-equilibrium status. The heat flux (J) was calculated as follows:

$$J = \frac{1}{V}\left[\sum_{i}^{N}\varepsilon_i v_i + \frac{1}{2}\sum_{ij;i\neq j}^{N}\left(F_{ij}\cdot v_i\right)\mathbf{r}_{ij} + \frac{1}{6}\sum_{ijk,i\neq j\neq k}^{N}\left(F_{ijk}\cdot v_i\right)\left(\mathbf{r}_{ij}+\mathbf{r}_{ik}\right)\right], \tag{1}$$

where ε_i is the energy; v_i represents the velocity of an atom i; r_{ij} is the interatomic distance between atoms i and j; F_{ij} and F_{ijk} are two-body and three-body forces, respectively; and V represents the volume of the investigated MoSSe/WSSe heterostructure. Furthermore, the calculated thickness of MoSSe and WSSe is 3.243 and 3.230 Å, respectively.

After obtaining the steady state for the systems, the temperature profile of the lateral MoSSe/WSSe heterostructure with an armchair and zigzag interface edge is demonstrated in **Figures 6A,B**, respectively. Reflection, transmission, and mode conversion occur by phonons travelling across the interface of the MoSSe/WSSe heterostructure, suggesting a temperature jump, which can further result in interfacial thermal resistance. Linear fitting and extrapolation were explored to calculate a more reasonable temperature jump (Yu and Zhang, 2013). As **Figure 6** shows, a significant temperature jump (ΔT) is characterized at the interface of the lateral MoSSe/WSSe heterostructure. Such a temperature jump is also obtained by other reported heterostructures, such as graphene/*h*-BN (Liu et al., 2016b), phosphorene/graphene (Liu et al., 2018), and MoS_2/WSe_2 (Qin et al., 2019). The heat flux of the arm-1, arm-2, zig-1, zig-2 MoSSe/WSSe heterostructures is calculated as 5.48×10^9, 6.21×10^9, 3.70×10^9, and 4.28×10^9 W m^{-2}, respectively. Besides, the temperature jump of the arm-1, arm-2, zig-1, and zig-2 MoSSe/WSSe heterostructures is obtained at 18.77, 14.66, 17.43 and 13.67 K, respectively. The interfacial thermal resistance (ITC) of the lateral MoSSe/WSSe heterostructure was decided as follows:

$$\lambda = \frac{J}{\Delta T}. \tag{2}$$

Therefore, pronounced ITC across the interfaces of the arm-1, arm-2, zig-1, and zig-2 MoSSe/WSSe heterostructures is 2.92×10^8, 4.24×10^8, 2.12×10^8, and 3.13×10^8 W K^{-1}·m^{-2}, respectively, which is comparable with that of graphene/BP (2.5×10^8 W K^{-1}·m^{-2}) (Liu et al., 2018). More importantly, the obtained ITC, 4.24×10^8 W K^{-1}·m^{-2}, of the arm-2 MoSSe/WSSe heterostructure is also larger than lateral heterostructure MoS_2/WSe_2 (3.65×10^8 W K^{-1}·m^{-2} and 3.76×10^8 W K^{-1}·m^{-2} along armchair and zigzag directions) (Qin et al., 2019). It is worth noting that the heat flux of arm-2 (or zig-2) is larger than that of the arm-1 (zig-1) MoSSe/WSSe heterostructure, which is suppressed by the interface bending in arm-1 (or zig-1).

In particular, it is observed that the heat flux of the arm-1 (arm-2) heterostructure is also higher than that of the zig-1 (zig-2) heterostructure. The phonon scattering spectrums of lateral MoSSe/WSSe heterostructures with armchair and zigzag interfaces are demonstrated in **Figures 7A,B**, respectively, obtained by the density functional theory by the unit cell, as

shown in **Figure 1**. It is worth noting that the slope of the acoustic branch in the arm-1 (or arm-2) heterostructure is steeper than that in the zig-1 (or zig-2) heterostructure in **Figure 7A** (or **Figure 7B**), which illustrates that the acoustic branches can be suppressed by the zigzag interface in the MoSSe/WSSe heterostructure, resulting in a lower group velocity. Thus, the heat flux in the MoSSe/WSSe heterostructure with an armchair interface is higher than that of the zigzag interface.

CONCLUSIONS

First-principles calculations and MD simulations were carried out to explore the electronic and thermal properties of the lateral Janus MoSSe/WSSe heterostructure. Four different structures of the Janus MoSSe/WSSe heterostructures were constructed by different symmetry and interface edges. These MoSSe/WSSe heterostructures possess direct type-II band structures, which can provide the ability to separate the photogenerated electrons and holes as a photocatalyst for water splitting. More interestingly, the asymmetric arrangement of S and Se in the Janus MoSSe/WSSe heterostructure can decrease the heat flux because of interface bending, while the lower heat flux and ITC of the Janus MoSSe/WSSe heterostructure with a zigzag interface is mainly due to the suppressed acoustic branches. The studied lateral Janus MoSSe/WSSe heterostructure in our work will provide theoretical guidance for the designing the 2D heterostructure to be used for future nano-devices.

DATA AVAILABILITY STATEMENT

The raw data supporting the conclusions of this article will be made available by the authors, without undue reservation.

AUTHOR CONTRIBUTIONS

All the authors listed have made a substantial, direct, and intellectual contribution to the work and approved it for publication.

FUNDING

The authors acknowledge the financial support for the research: Zhejiang Basic Public Welfare Research Program (Grant number: LGG20E050001), Academic Support Project for Top Talents of Subjects (majors) in Colleges and Universities (Grant number: gxbjZD63), Key Project of Natural Science Research of the Anhui Provincial Department of Education (Grant number: KJ 2019A1140), and School Level Scientific Research Promotion Plan Project (Grant number: ZXTS201801).

REFERENCES

Agarwal, A., Goverapet Srinivasan, S., and Rai, B. (2021). Data Driven Discovery of 2D Materials for Solar Water Splitting. *Front. Mater.* 8, 292. doi:10.3389/fmats.2021.679269

Allain, A., and Kis, A. (2014). Electron and Hole Mobilities in Single-Layer WSe2. *ACS Nano* 8, 7180–7185. doi:10.1021/nn5021538

Ang, Y. S., and Ang, L. K. (2019). Theory of Thermionic Carrier Injection in Graphene/organic Schottky Interface. *Front. Mater.* 6, 204. doi:10.3389/fmats.2019.00204

Butler, S. Z., Hollen, S. M., Cao, L., Cui, Y., Gupta, J. A., Gutiérrez, H. R., et al. (2013). Progress, Challenges, and Opportunities in Two-Dimensional Materials Beyond Graphene. *ACS Nano* 7, 2898–2926. doi:10.1021/nn400280c

Capelle, K. (2006). A Bird's-Eye View of Density-Functional Theory. *Braz. J. Phys.* 36, 1318–1343. doi:10.1590/s0103-97332006000700035

Chen, X.-K., Zeng, Y.-J., and Chen, K.-Q. (2020). Thermal Transport in Two-Dimensional Heterostructures. *Front. Mater.*, 427. doi:10.3389/fmats.2020.578791

Cui, Z., Luo, Y., Yu, J., and Xu, Y. (2021). Tuning the Electronic Properties of MoSi2N4 by Molecular Doping: A First Principles Investigation. *Physica E: Low-dimensional Syst. Nanostructures* 134, 114873. doi:10.1016/j.physe.2021.114873

Cui, Z., Lyu, N., Ding, Y., and Bai, K. (2021). Noncovalently Functionalization of Janus MoSSe Monolayer with Organic Molecules. *Physica E: Low-dimensional Syst. Nanostructures* 127, 114503. doi:10.1016/j.physe.2020.114503

Ding, G., He, J., Gao, G. Y., and Yao, K. (2018). Two-dimensional MoS_2-$MoSe_2$ Lateral Superlattice with Minimized Lattice Thermal Conductivity. *J. Appl. Phys.* 124. doi:10.1063/1.5051067

Dongqi, S., Xinjian, L., Ying, Z., Min, Z., and Xinyi, H. (2021). Structural and Transport Properties of 1T-VSe_2 Single crystal Under High Pressures. *Front. Mater.* 8, 710849. doi:10.3389/fmats.2021.710849

Duan, X., Wang, C., Shaw, J. C., Cheng, R., Chen, Y., Li, H., et al. (2014). Lateral Epitaxial Growth of Two-Dimensional Layered Semiconductor Heterojunctions. *Nat. Nanotech* 9, 1024–1030. doi:10.1038/nnano.2014.222

Fan, Q., Yan, L., Tripp, M. W., Krejčí, O., Dimosthenous, S., Kachel, S. R., et al. (2021). Biphenylene Network: A Nonbenzenoid Carbon Allotrope. *Science* 372, 852–856. doi:10.1126/science.abg4509

Gao, Y., Jing, Y., Liu, J., Li, X., and Meng, Q. (2017). Tunable Thermal Transport Properties of Graphene by Single-Vacancy Point Defect. *Appl. Therm. Eng.* 113, 1419–1425. doi:10.1016/j.applthermaleng.2016.11.160

Geim, A. K., and Novoselov, K. S. (2010). "The Rise of Graphene," in *Nanoscience and Technology: A Collection of Reviews from Nature Journals* (World Scientific), 11–19.

Guo, W., Ge, X., Sun, S., Xie, Y., and Ye, X. (2020). The Strain Effect on the Electronic Properties of the MoSSe/WSSe van der Waals Heterostructure: A First-principles Study. *Phys. Chem. Chem. Phys.* 22, 4946–4956. doi:10.1039/d0cp00403k

Hidding, J., and Guimarães, M. H. (2020). Spin-Orbit Torques in Transition Metal Dichalcogenides/Ferromagnet Heterostructures. *Front. Mater.* 7, 383. doi:10.3389/fmats.2020.594771

Hong, Y.-L., Liu, Z., Wang, L., Zhou, T., Ma, W., Xu, C., et al. (2020). Chemical Vapor Deposition of Layered Two-Dimensional MoSi 2 N 4 Materials. *Science* 369, 670–674. doi:10.1126/science.abb7023

Hu, Y., Feng, T., Gu, X., Fan, Z., Wang, X., Lundstrom, M., et al. (2020). Unification of Nonequilibrium Molecular Dynamics and the Mode-Resolved Phonon Boltzmann Equation for Thermal Transport Simulations. *Phys. Rev. B* 101, 155308. doi:10.1103/physrevb.101.155308

Jiang, J.-W. (2018). Misfit Strain-Induced Buckling for Transition-Metal Dichalcogenide Lateral Heterostructures: A Molecular Dynamics Study. *Acta Mech. Solida Sin.* 32, 17–28. doi:10.1007/s10338-018-0049-z

Jo, S.-H., Lee, H. W., Shim, J., Heo, K., Kim, M., Song, Y. J., et al. (2018). Highly Efficient Infrared Photodetection in a Gate-Controllable Van der Waals Heterojunction with Staggered Bandgap Alignment. *Adv. Sci.* 5, 1700423. doi:10.1002/advs.201700423

Keyte, J., Pancholi, K., and Njuguna, J. (2019). Recent Developments in Graphene Oxide/epoxy Carbon Fiber-Reinforced Composites. *Front. Mater.* 6, 224. doi:10.3389/fmats.2019.00224

Kim, D.-H., Kim, M.-S., and Kim, H.-D. (2015). Geometrical and Electronic Structures of Graphene Under Different Vacancy Density and Configuration. *Appl. Surf. Sci.* 359, 55–60. doi:10.1016/j.apsusc.2015.10.055

Kresse, G., and Furthmüller, J. (1996). Efficient Iterative Schemes Forab Initiototal-Energy Calculations Using a Plane-Wave Basis Set. *Phys. Rev. B* 54, 11169–11186. doi:10.1103/physrevb.54.11169

Kresse, G., and Joubert, D. (1999). From Ultrasoft Pseudopotentials to the Projector Augmented-Wave Method. *Phys. Rev. B* 59, 1758–1775. doi:10.1103/physrevb.59.1758

Li, F., Wei, W., Zhao, P., Huang, B., and Dai, Y. (2017). Electronic and Optical Properties of Pristine and Vertical and Lateral Heterostructures of Janus MoSSe and WSSe. *J. Phys. Chem. Lett.* 8, 5959–5965. doi:10.1021/acs.jpclett.7b02841

Li, J., Huang, Z., Ke, W., Yu, J., Ren, K., and Dong, Z. (2021). High Solar-to-hydrogen Efficiency in Arsenene/GaX (X = S, Se) van der Waals Heterostructure for Photocatalytic Water Splitting. *J. Alloys Comp.* 866, 158774. doi:10.1016/j.jallcom.2021.158774

Li, L., Yu, Y., Ye, G. J., Ge, Q., Ou, X., Wu, H., et al. (2014). Black Phosphorus Field-Effect Transistors. *Nat. Nanotech* 9, 372–377. doi:10.1038/nnano.2014.35

Li, L., Zhou, M., Jin, L., Liu, L., Mo, Y., Li, X., et al. (2019). Research Progress of the Liquid-phase Exfoliation and Stable Dispersion Mechanism and Method of Graphene. *Front. Mater.* 6, 325. doi:10.3389/fmats.2019.00325

Liu, X., Gao, J., Zhang, G., and Zhang, Y. W. (2018). Design of Phosphorene/graphene Heterojunctions for High and Tunable Interfacial Thermal Conductance. *Nanoscale* 10, 19854–19862. doi:10.1039/c8nr06110f

Liu, X., Zhang, G., and Zhang, Y.-W. (2016). Topological Defects at the Graphene/h-BN Interface Abnormally Enhance its Thermal Conductance. *Nano Lett.* 16, 4954–4959. doi:10.1021/acs.nanolett.6b01565

Liu, Y., Weiss, N. O., Duan, X., Cheng, H.-C., Huang, Y., and Duan, X. (2016). Van der Waals Heterostructures and Devices. *Nat. Rev. Mater.* 1, 16042. doi:10.1038/natrevmats.2016.42

Lou, J., Ren, K., Huang, Z., Huo, W., Zhu, Z., and Yu, J. (2021). Electronic and Optical Properties of Two-Dimensional Heterostructures Based on Janus XSSe (X = Mo, W) and Mg(OH)2: A First Principles Investigation. *RSC Adv.* 11, 29576–29584. doi:10.1039/d1ra05521f

Lu, A.-Y., Zhu, H., Xiao, J., Chuu, C.-P., Han, Y., Chiu, M.-H., et al. (2017). Janus Monolayers of Transition Metal Dichalcogenides. *Nat. Nanotech* 12, 744–749. doi:10.1038/nnano.2017.100

Luo, Y., Ren, C., Xu, Y., Yu, J., Wang, S., and Sun, M. (2021). A First Principles Investigation on the Structural, Mechanical, Electronic, and Catalytic Properties of Biphenylene. *Sci. Rep.* 11, 19008. doi:10.1038/s41598-021-98261-9

Luo, Y., Ren, K., Wang, S., Chou, J.-P., Yu, J., Sun, Z., et al. (2019). First-Principles Study on Transition-Metal Dichalcogenide/BSe van der Waals Heterostructures: A Promising Water-Splitting Photocatalyst. *J. Phys. Chem. C* 123, 22742–22751. doi:10.1021/acs.jpcc.9b05581

Luo, Y., Wang, S., Ren, K., Chou, J.-P., Yu, J., Sun, Z., et al. (2019). Transition-metal Dichalcogenides/Mg(OH)2 van der Waals Heterostructures as Promising Water-splitting Photocatalysts: A First-principles Study. *Phys. Chem. Chem. Phys.* 21, 1791–1796. doi:10.1039/c8cp06960c

Ma, Y., Dai, Y., Guo, M., Niu, C., Lu, J., and Huang, B. (2011). Electronic and Magnetic Properties of Perfect, Vacancy-Doped, and Nonmetal Adsorbed MoSe2, MoTe2 and WS2 Monolayers. *Phys. Chem. Chem. Phys.* 13, 15546–15553. doi:10.1039/c1cp21159e

Novoselov, K. S., Mishchenko, A., Carvalho, A., and Castro Neto, A. H. (2016). 2D Materials and van der Waals Heterostructures. *Science* 353, aac9439. doi:10.1126/science.aac9439

Ong, W.-J. (2017). 2D/2D Graphitic Carbon Nitride (G-C3n4) Heterojunction Nanocomposites for Photocatalysis: Why Does Face-To-Face Interface Matter. *Front. Mater.* 4, 11. doi:10.3389/fmats.2017.00011

Ouyang, T., Wang, X., Liu, S., Chen, H., and Deng, S. (2021). A Complete Two-Dimensional Avalanche Photodiode Based on $MoTe_2$–WS_2–$MoTe_2$ Heterojunctions with Ultralow Dark Current. *Front. Mater.* 8, 736180. doi:10.3389/fmats.2021.736180

Perdew, J. P., Burke, K., and Ernzerhof, M. (1996). Generalized Gradient Approximation Made Simple. *Phys. Rev. Lett.* 77, 3865–3868. doi:10.1103/physrevlett.77.3865

Plimpton, S. (1995). Fast Parallel Algorithms for Short-Range Molecular Dynamics. *J. Comput. Phys.* 117, 1–19. doi:10.1006/jcph.1995.1039

Qin, H., Pei, Q.-X., Liu, Y., and Zhang, Y.-W. (2019). The Mechanical and Thermal Properties of MoS2-WSe2 Lateral Heterostructures. *Phys. Chem. Chem. Phys.* 21, 15845–15853. doi:10.1039/c9cp02499a

Ren, K., Liu, X., Chen, S., Cheng, Y., Tang, W., and Zhang, G. (2020). Remarkable Reduction of Interfacial Thermal Resistance in Nanophononic Heterostructures. *Adv. Funct. Mater.* 30, 2004003. doi:10.1002/adfm.202004003

Ren, K., Shu, H., Huo, W., Cui, Z., Yu, J., and Xu, Y. (2021). Mechanical, Electronic and Optical Properties of a Novel B2P6 Monolayer: Ultrahigh Carrier Mobility and Strong Optical Absorption. *Phys. Chem. Chem. Phys.* 23, 24915–24921. doi:10.1039/d1cp03838a

Ren, K., Sun, M., Luo, Y., Wang, S., Yu, J., and Tang, W. (2019). First-principle Study of Electronic and Optical Properties of Two-Dimensional Materials-Based Heterostructures Based on Transition Metal Dichalcogenides and Boron Phosphide. *Appl. Surf. Sci.* 476, 70–75. doi:10.1016/j.apsusc.2019.01.005

Ren, K., Tang, W., Sun, M., Cai, Y., Cheng, Y., and Zhang, G. (2020). A Direct Z-scheme PtS2/arsenene van der Waals Heterostructure with High Photocatalytic Water Splitting Efficiency. *Nanoscale* 12, 17281–17289. doi:10.1039/d0nr02286a

Ren, K., Wang, S., Luo, Y., Chou, J.-P., Yu, J., Tang, W., et al. (2020). High-efficiency Photocatalyst for Water Splitting: A Janus MoSSe/XN (X = Ga, Al) van der Waals Heterostructure. *J. Phys. D: Appl. Phys.* 53, 185504. doi:10.1088/1361-6463/ab71ad

Ren, K., Yu, J., and Tang, W. (2020). Two-dimensional ZnO/BSe van der waals Heterostructure Used as a Promising Photocatalyst for Water Splitting: A DFT Study. *J. Alloys Comp.* 812, 152049. doi:10.1016/j.jallcom.2019.152049

Ren, K., Zheng, R., Lou, J., Yu, J., Sun, Q., and Li, J. (2021). Ab Initio Calculations for the Electronic, Interfacial and Optical Properties of Two-Dimensional AlN/Zr2CO2 Heterostructure. *Front. Chem.* 9, 796695. doi:10.3389/fchem.2021.796695

Ren, K., Zheng, R., Xu, P., Cheng, D., Huo, W., Yu, J., et al. (2021). Electronic and Optical Properties of Atomic-Scale Heterostructure Based on MXene and MN (M = Al, Ga): A DFT Investigation. *Nanomaterials* 11, 2236. doi:10.3390/nano11092236

Ren, K., Zheng, R., Yu, J., Sun, Q., and Li, J. (2021). Band Bending Mechanism in CdO/Arsenene Heterostructure: A Potential Direct Z-Scheme Photocatalyst. *Front. Chem.* 9, 788813. doi:10.3389/fchem.2021.788813

Shi, Y., Hua, C., Li, B., Fang, X., Yao, C., Zhang, Y., et al. (2013). Highly Ordered Mesoporous Crystalline MoSe2Material with Efficient Visible-Light-Driven Photocatalytic Activity and Enhanced Lithium Storage Performance. *Adv. Funct. Mater.* 23, 1832–1838. doi:10.1002/adfm.201202144

Shu, H. (2021). Adjustable Electro-Optical Properties of Novel Graphene-like SiC_2 via Strain Engineering. *Appl. Surf. Sci.* 559. doi:10.1016/j.apsusc.2021.149956

Sun, M., Chou, J.-P., Hu, A., and Schwingenschlögl, U. (2019). Point Defects in Blue Phosphorene. *Chem. Mater.* 31, 8129–8135. doi:10.1021/acs.chemmater.9b02871

Sun, M., Chou, J.-P., Ren, Q., Zhao, Y., Yu, J., and Tang, W. (2017). Tunable Schottky Barrier in van der Waals Heterostructures of Graphene and g-GaN. *Appl. Phys. Lett.* 110, 173105. doi:10.1063/1.4982690

Sun, M., Luo, Y., Yan, Y., and Schwingenschlögl, U. (2021). Ultrahigh Carrier Mobility in the Two-Dimensional Semiconductors B8Si4, B8Ge4, and B8Sn4. *Chem. Mater.* 33, 6475–6483. doi:10.1021/acs.chemmater.1c01824

Sun, M., and Schwingenschlögl, U. (2020). B2P6: A Two-Dimensional Anisotropic Janus Material with Potential in Photocatalytic Water Splitting and Metal-Ion Batteries. *Chem. Mater.* 32, 4795–4800. doi:10.1021/acs.chemmater.0c01536

Sun, M., and Schwingenschlögl, U. (2021). Structure Prototype Outperforming MXenes in Stability and Performance in Metal-Ion Batteries: A High Throughput Study. *Adv. Energ. Mater.* 11, 2003633. doi:10.1002/aenm.202003633

Sun, M., and Schwingenschlögl, U. (2021). Unique Omnidirectional Negative Poisson's Ratio in δ-Phase Carbon Monochalcogenides. *J. Phys. Chem. C* 125, 4133–4138. doi:10.1021/acs.jpcc.0c11555

Sun, M., Schwingenschlögl, U., and δ-, C. S. (2020). A Direct-Band-Gap Semiconductor Combining Auxeticity, Ferroelasticity, and Potential for High-Efficiency Solar Cells. *Phys. Rev. Appl.* 14, 044015. doi:10.1103/physrevapplied.14.044015

Togo, A., Oba, F., and Tanaka, I. (2008). First-principles Calculations of the Ferroelastic Transition Between Rutile-type and CaCl2-typeSiO2 at High Pressures. *Phys. Rev. B* 78, 134106. doi:10.1103/physrevb.78.134106

Togo, A., and Tanaka, I. (2015). First Principles Phonon Calculations in Materials Science. *Scripta Materialia* 108, 1–5. doi:10.1016/j.scriptamat.2015.07.021

Trivedi, D. B., Turgut, G., Qin, Y., Sayyad, M. Y., Hajra, D., Howell, M., et al. (2020). Room-Temperature Synthesis of 2D Janus Crystals and Their Heterostructures. *Adv. Mater.* 32, e2006320. doi:10.1002/adma.202006320

Vahedi Fakhrabad, D., Shahtahmasebi, N., and Ashhadi, M. (2015). Optical Excitations and Quasiparticle Energies in the AlN Monolayer Honeycomb Structure. *Superlattices and Microstructures* 79, 38–44. doi:10.1016/j.spmi.2014.12.012

Wang, B., Wang, X., Wang, P., Yang, T., Yuan, H., Wang, G., et al. (2019). Bilayer MoSe2/HfS2 Nanocomposite as a Potential Visible-Light-Driven Z-Scheme Photocatalyst. *Nanomaterials* 9, 1706. doi:10.3390/nano9121706

Wang, G., Zhang, L., Li, Y., Zhao, W., Kuang, A., Li, Y., et al. (2019). Biaxial Strain Tunable Photocatalytic Properties of 2D ZnO/GeC Heterostructure. *J. Phys. D: Appl. Phys.* 53, 015104. doi:10.1088/1361-6463/ab440e

Wei, N., Chen, Y., Cai, K., Zhao, J., Wang, H.-Q., and Zheng, J.-C. (2016). Thermal Conductivity of Graphene Kirigami: Ultralow and Strain Robustness. *Carbon* 104, 203–213. doi:10.1016/j.carbon.2016.03.043

Xu, Q., Zhang, L., Yu, J., Wageh, S., Al-Ghamdi, A. A., and Jaroniec, M. (2018). Direct Z-Scheme Photocatalysts: Principles, Synthesis, and Applications. *Mater. Today* 21, 1042–1063. doi:10.1016/j.mattod.2018.04.008

Xu, W., Zhang, G., and Li, B. (2015). Thermal Conductivity of Penta-Graphene from Molecular Dynamics Study. *J. Chem. Phys.* 143, 154703. doi:10.1063/1.4933311

Xu, Y., Lu, F., Liu, K., and Ma, C. (2020). Direct Graphene Synthesis on Lithium Niobate Substrate by Carbon Ion Implantation. *Front. Mater.* 7, 327. doi:10.3389/fmats.2020.572280

Yu, C., and Zhang, G. (2013). Impacts of Length and Geometry Deformation on thermal Conductivity of Graphene Nanoribbons. *J. Appl. Phys.* 113, 044306. doi:10.1063/1.4788813

Zaminpayma, E., Razavi, M. E., and Nayebi, P. (2017). Electronic Properties of Graphene with Single Vacancy and Stone-Wales Defects. *Appl. Surf. Sci.* 414, 101–106. doi:10.1016/j.apsusc.2017.04.065

Zhang, H., Chhowalla, M., and Liu, Z. (2018). 2D Nanomaterials: Graphene and Transition Metal Dichalcogenides. *Chem. Soc. Rev.* 47, 3015–3017. doi:10.1039/c8cs90048e

Zhao, H., Li, E., Liu, C., Shen, Y., Shen, P., Cui, Z., et al. (2021). DFT Computation of Two-dimensional CdO/GaS van der Waals Heterostructure: Tunable Absorption Spectra for Water Splitting Application. *Vacuum* 192, 110434. doi:10.1016/j.vacuum.2021.110434

Zhao, W., Ghorannevis, Z., Chu, L., Toh, M., Kloc, C., Tan, P.-H., et al. (2013). Evolution of Electronic Structure in Atomically Thin Sheets of WS2 and WSe2. *ACS Nano* 7, 791–797. doi:10.1021/nn305275h

Zhou, Q., Yong, Y., Su, X., Ju, W., Fu, Z., and Li, X. (2018). Adsorption Behavior of O2 on Vacancy-Defected Graphene with Transition-Metal Dopants: A Theoretical Study. *Int. J. Mod. Phys. B* 32, 1850304. doi:10.1142/s0217979218503046

Conflict of Interest: The authors declare that the research was conducted in the absence of any commercial or financial relationships that could be construed as a potential conflict of interest.

Publisher's Note: All claims expressed in this article are solely those of the authors and do not necessarily represent those of their affiliated organizations, or those of the publisher, the editors, and the reviewers. Any product that may be evaluated in this article, or claim that may be made by its manufacturer, is not guaranteed or endorsed by the publisher.